Chapter 5

Optical Loss and Lasing Characteristics of AlGaAs Microdisk Cavities with Embedded Quantum Dots

5.1 Introduction

For future experiments in cavity QED with self-assembled quantum dots, the GaAs/AlGaAs system is the most appropriate choice of material, due to the relative maturity of the growth of InAs/InGaAs quantum dots [138, 139, 140] within this system. As the refractive index of GaAs and its alloys is relatively close to that of Si ($n_{GaAs} \sim 3.5$ and $n_{AlAs} \sim 2.9$ at $\lambda \sim 1.25$ μm), the PC cavity design of chapter 2 remains applicable. Similarly, the high refractive index difference between GaAs/AlGaAs and air suggests that the radiation-limited Qs for microdisk cavities would be quite high for all but the smallest diameter disks. At the start of the work described in this chapter, what remained to be seen was whether the fabrication processes and material losses within this new system would be adequate to achieve a sufficiently high Q and small $V_{\rm eff}$ for strong coupling experiments.

Recently, multiple research groups have demonstrated vacuum Rabi splitting in a semiconductor system consisting of a single quantum dot (QD) exciton embedded in an optical microcavity [70, 71, 72]. These experiments have in many ways confirmed the potential of semiconductor microcavities for chip-based cavity quantum electrodynamics (cQED) experiments. For future experiments, such as those involving quantum state transfer in quantum networks [141], it will be important to further improve upon the parameters of such QD-microcavity systems over what was demonstrated in the above references. One clear improvement required is to move the system further within the regime of strong coupling. In particular, the ratio of g (the QD-photon coupling rate) to the larger of κ (the cavity decay rate) and $\gamma_\perp$ (the QD decay rate) approximately represents the number of Rabi

oscillations that can take place before the effects of dissipation destroy coherent energy exchange [9]. In each of refs. [70, 71, 72], loss in the system was found to be dominated by the optical cavity, with $g \lesssim \kappa$. As the low-temperature homogeneous linewidth in self-assembled InAs QDs is typically a few μeV [142], corresponding to a QD dipole decay rate of $\gamma_\perp/2\pi \sim 1$ GHz, it will be advantageous to develop cavities with quality factors such that $\kappa/2\pi \lesssim 1$ GHz, with further improvements in Q serving mainly to improve the optical collection efficiency of emitted light. For the $\lambda \sim 0.9$-1.2 μm emission wavelength for InAs QDs [70, 71], this corresponds to an optical mode quality factor of $Q \sim 1\times10^5$ ($\kappa/2\pi = \omega/4\pi Q$). Achieving such low loss cavities is also important in light of the difficulty in fabricating a structure where the QD is optimally positioned for maximum coupling to the cavity mode.

In this chapter, we review results first presented in ref. [69], which details the creation of D=4.5 μm diameter AlGaAs microdisks that exhibit Q factors as high as 3.6×10^5 at $\lambda \sim 1.4$ μm, a value which, to our knowledge, exceeds the highest Q factors measured for AlGaAs microcavities to date [13, 14, 70, 71]. These AlGaAs microdisks contain embedded quantum dots-in-a-well (DWELL) [143, 144] that have a ground state emission at $\lambda \sim 1.2$ μm, so that passive, fiber-taper-based measurements are performed at $\lambda \sim 1.4$ μm, where the QDs are relatively non-absorbing. The characteristics of these devices are also investigated through photoluminescence measurements, and low threshold, room temperature QD lasers are demonstrated.

5.2 Overview of microdisk cavity modes

5.2.1 Analytic approximation

In a perfectly circular microdisk structure, the cavity modes circulate around the periphery of the device in traveling wave whispering gallery modes (WGMs). These WGMs are classified in terms of their polarization (TE or TM), radial order (p), and azimuthal number (m).[1] Unlike microspheres, where the WGMs can be solved for analytically, microdisk modes do not have an analytic solution. An approximate analytic solution can be easily found, however, and yields physical insight into the properties of these modes. Such an approach has been considered by many authors; here, I follow the derivation of Borselli et al., in ref. [65].

We begin with Maxwell's equations in a charge-free, current-free medium:

[1] As the microdisks studied here are optically thin, only the first order TE and TM modes are considered.

$$\begin{aligned} \nabla \times \mathbf{E} &= -i\omega\mu_0\mathbf{H}, \\ \nabla \times \mathbf{H} &= +i\omega n^2\varepsilon_0\mathbf{E}, \\ \boldsymbol{\nabla} \cdot (n^2\varepsilon_0\mathbf{E}) &= 0, \\ \nabla \cdot \boldsymbol{\mu_0}\mathbf{H} &= 0, \end{aligned} \tag{5.1}$$

where we have assumed that the fields oscillate in time as $\exp(i\omega t)$. For a piecewise homogeneous medium, these equations can be used to derive the familiar wave equations:

$$\begin{aligned} \boldsymbol{\nabla}^2\mathbf{E} + \frac{n^2\omega^2}{c^2}\mathbf{E} &= 0 \\ \boldsymbol{\nabla}^2\mathbf{H} + \frac{n^2\omega^2}{c^2}\mathbf{H} &= 0 \end{aligned} \tag{5.2}$$

As the form of equation (5.2) is the same for both **E** and **H**, from here on out we write everything in terms of a single vector field **F**, which can stand for either of the two. In cylindrical coordinates (ρ,ϕ,z), we can re-write this as:

$$\left(\frac{\partial^2}{\partial\rho^2} + \frac{1}{\rho}\frac{\partial}{\partial\rho} + \frac{1}{\rho^2}\frac{\partial^2}{\partial\phi^2} + \frac{\partial^2}{\partial z^2} + \left(\frac{\omega}{c}\right)^2\right)\mathbf{F} = 0 \tag{5.3}$$

We now invoke the major approximation used, which is to separate the modes into TE and TM polarizations, which contain the field components $\{E_\rho, E_\phi, H_z\}$ and $\{H_\rho, H_\phi, E_z\}$, respectively. For actual structures, this separation is only approximate (it truly only holds within the center of the slab WG). It provides the significant simplification of making equation (5.3) a scalar wave equation in F_z, where F_z is H_z (E_z) for TE (TM) modes. We then use separation of variables [145] with $F_z = \Psi(\rho)\Omega(\phi)Z(z)$ to break up equation (5.3) into three equations, given as:

$$\begin{aligned} \frac{\partial^2\Omega}{\partial\phi^2} + m^2\Omega &= 0 \\ \frac{\partial^2 Z}{\partial z^2} + \frac{\omega^2}{c^2}(n^2 - \bar{n}^2)Z &= 0 \\ \frac{\partial^2\Psi}{\partial\rho^2} + \frac{1}{\rho}\frac{\partial\Psi}{\partial\rho} + \left(\frac{\omega^2\bar{n}^2}{c^2} - \frac{m^2}{\rho^2}\right)\Psi &= 0 \end{aligned} \tag{5.4}$$

where $\bar{n}$ is the effective index. The first equation can immediately be solved, giving the azimuthal dependence $\Omega(\phi) = \exp(im\phi)$, where m is the azimuthal mode number (eigenvalue). The second equation is nothing more than the standard equation for the mode of a slab waveguide, as discussed in detail within ref. [126], for example. The third equation is used to solve for the radial dependence of the cavity mode. The solutions to this equation are Bessel functions within the disk ($\rho < R$, where R is the disk radius), and Hankel functions outside of it ($\rho > R$). As discussed in ref. [65], the Hankel function solution can be approximated by a decaying exponential, so that the radial solution $\Psi(\rho)$ has the form:

$$\Psi(\rho) = \begin{cases} J_m(\frac{\omega}{c}\bar{n}\rho), & \rho \leq R \\ J_m(\frac{\omega}{c}\bar{n}R)\exp(-\alpha(\rho - R)), & \rho \geq R. \end{cases} \tag{5.5}$$

The decay constant α is given as $\alpha = \frac{\omega}{c}(\bar{n}^2 - {n_0}^2)^{1/2}$ (n_0=1 for an air-clad disk). Finally, the azimuthal mode number m is determined (for a given frequency ω, disk radius R, and effective index $\bar{n}$) by the boundary conditions on the fields at $\rho = R$. This yields the transcendental equation:

$$\frac{\omega}{c}\bar{n}J_{m+1}(\frac{\omega}{c}\bar{n}R) = \left(\frac{m}{R} + \eta\alpha\right)J_m(\frac{\omega}{c}\bar{n}R) \tag{5.6}$$

where $\eta = \bar{n}^2/n_0^2$ for a TE mode and $\eta = 1$ for a TM mode.

For very rough estimates, a back of the envelope calculation of m can be useful. One that is typically used is to require that m wavelengths fit in the circumference of the disk. Written explicitly, this is stated as:

$$m\frac{\lambda_m}{n_g} = 2\pi R \tag{5.7}$$

where λ_m is the resonant wavelength of mode m, and n_g is the group index of the waveguide mode, which can be determined from the slope of the waveguide dispersion curve (through solving the slab waveguide portion of equation (5.4) for ω as a function of β=$\bar{n}\omega/c$). The free spectral range (FSR), which gives the separation between adjacent modes, is then:

$$\Delta\nu = \nu_{m+1} - \nu_m = \frac{c}{2\pi R n_g} \tag{5.8}$$

This is nothing more than the standard equation for the FSR of a Fabry-Perot cavity with the round-trip length of the cavity equal to the circumference of the microdisk.

5.2.2 Finite-element method simulations

To quantitatively study the properties of the microdisk cavities, we use finite-element eigenfrequency simulations based on the Comsol FEMLAB commercial software. The specific implementation I have used is based on the work of Matt Borselli [128, 137], who in turn received assistance from Sean Spillane [136]. By assuming azimuthal symmetry of the disk structures, only a two-dimensional cross section of the disk is simulated, albeit using a full-vectorial model. That is, the explicit azimuthal symmetry package offered within the software is not appropriate, because it forces the calculated modes to be azimuthally symmetric (i.e., m=0). Instead, we essentially solve the wave equation (5.3) assuming an azimuthal dependence of $\exp(im\phi)$. We seek solutions close to some nominal wavelength λ_{nom}, and specify an m value as found by solution of the transcendental equation (5.6). The FEMLAB solver then determines the precise frequency λ_0 at which the mode of azimuthal number m occurs. It also provides the spatial mode profile, which is used to calculate the cavity mode effective volume according to the already-mentioned formula:

$$V_{\text{eff}} = \frac{\int_V \varepsilon(\mathbf{r})|\mathbf{E}(\mathbf{r})|^2 d^3\mathbf{r}}{\max[\varepsilon(\mathbf{r})|\mathbf{E}(\mathbf{r})|^2]} \tag{5.9}$$

where $\varepsilon(\mathbf{r})$ is the dielectric constant, $|E(\mathbf{r})|$ is the electric field strength, and V is a quantization volume encompassing the resonator and with a boundary in the radiation zone of the cavity mode under study. The resonance wavelength λ_0 and radiation limited quality factor Q_{rad} are determined from the complex eigenvalue (wavenumber) of the resonant cavity mode, k, obtained by the finite-element solver, with $\lambda_0 = 2\pi/\mathfrak{Re}(k)$ and $Q_{\text{rad}} = \mathfrak{Re}(k)/(2\mathfrak{Im}(k))$. For the microdisks studied in this chapter and in chapter 6, Q_{rad} is quite large ($> 10^{14}$), and the finite element simulations are only sparingly used. In chapter 7, however, we consider small enough diameter structures that Q_{rad} is a significant contributor to the overall Q of the devices. We will therefore consider these simulations

in greater detail within that chapter.

5.2.3 Standing wave whispering gallery modes

For the devices studied in this thesis, the high-Q modes are not traveling waves but are instead standing waves. This is a result of coherent coupling between the forwards and backwards propagating disk modes (i.e., modes of azimuthal number $\pm m$) as a result of surface roughness. The key behind this coherent coupling is that the modal loss (due to factors such as absorption, scattering, radiation, etc.) is low enough that the backscattering rate caused by the surface roughness is significant in comparison to it.

This modal coupling has been observed experimentally and explained by many other authors, including those of refs. [146, 147, 148, 135, 64]. Here, we present a simple analysis of this coupling. This analysis is essentially an abridged version of that which appears in a recent paper by Borselli et al. [65].

Maxwell's wave equation for the electric field vector in the microdisk structure is

$$\nabla^2\mathbf{E} - \mu_0\left(\varepsilon^0 + \delta\varepsilon\right)\frac{\partial^2\mathbf{E}}{\partial t^2} = 0, \tag{5.10}$$

where μ_0 is the permeability of free space, ε^0 is the dielectric function for the ideal microdisk and $\delta\varepsilon$ is the dielectric perturbation that is the source of mode coupling between the *cw* and *ccw* modes. Assuming a harmonic time dependence, the modes of the ideal structure are written as $\mathbf{E}_j^0(\mathbf{r},t) = \mathbf{E}_j^0(\mathbf{r})\exp(i\omega_j t)$, and are solutions of equation 5.10 with $\delta\varepsilon = 0$. Solutions to equation (5.10) with $\delta\varepsilon \neq 0$ (i.e., modes of the perturbed structure) are assumed to be written as

$$\mathbf{E}(\mathbf{r},t) = e^{-i\omega_0 t}\sum_j a_j(t)\mathbf{E}_j^0(\mathbf{r}). \tag{5.11}$$

Plugging into equation (5.10), keeping only terms up to first order, and utilizing mode orthogonality, we arrive at the coupled mode equations

$$\frac{da_k}{dt} + i\Delta\omega_k a_k(t) = i\sum_j \beta_{jk} a_j(t) \tag{5.12}$$

$$\beta_{jk} = \frac{\omega_0}{2} \frac{\int \delta\varepsilon \left(\mathbf{E}_j^0(\mathbf{r})\right)^* \mathbf{E}_k^0((r))d\mathbf{r}}{\int \varepsilon^0 |\mathbf{E}_k^0(\mathbf{r})|^2 d\mathbf{r}}. \tag{5.13}$$

Reference [65] presents a functional form for β in situations involving a small amount of surface roughness. We now explicitly assume that only two modes (the *cw* and *ccw* modes of a given polarization (TE or TM), azimuthal mode number *m*, and radial mode number *p*) are involved, and that the amplitude of the backscattering rates are equal, so that $|\beta_{cw,ccw}| = |\beta_{ccw,cw}| = |\beta|$. The coupled mode equations then read as

$$\frac{da_{cw}}{dt} = -i\Delta\omega a_{cw}(t) + i|\beta|e^{i\xi} a_{ccw}(t) \tag{5.14}$$

$$\frac{da_{ccw}}{dt} = -i\Delta\omega a_{ccw}(t) + i|\beta|e^{-i\xi} a_{cw}(t), \tag{5.15}$$

where we have taken $\beta = |\beta|e^{i\xi}$. These equations represent the time evolution of the two mode amplitudes (a_{cw},a_{ccw}) of an isolated system, without loss or coupling to an external waveguide. The inclusion of such terms will be considered later in this thesis, in chapter 8.

These two coupled equations can be uncoupled by introducing the variables $a_{sw,1}$ and $a_{sw,2}$, which represent the standing wave mode amplitudes:

$$a_{sw,1} = \frac{1}{\sqrt{2}}\left(a_{cw} + e^{i\xi} a_{ccw}\right) \tag{5.16}$$

$$a_{sw,2} = \frac{1}{\sqrt{2}}\left(a_{cw} - e^{i\xi} a_{ccw}\right). \tag{5.17}$$

As we saw earlier within this chapter, for an ideal microdisk, a_{cw} and a_{ccw} have an azimuthal spatial dependence of $e^{im\phi}$ (where *m* is the azimuthal mode number and is a nonzero integer), so that $a_{sw,1}$ and $a_{sw,2}$ will have an azimuthal spatial dependence that will be a mixture of $\cos(m\phi)$ and $\sin(m\phi)$, with the precise dependence being a function of the phase ξ of the backscattering parameter β. Rewriting the coupled mode equations in terms of the standing wave mode amplitudes, we arrive at:

$$\frac{da_{sw,1}}{dt} = -i\Delta\omega a_{sw,1}(t) + i|\beta|a_{sw,1}(t), \tag{5.18}$$

$$\frac{da_{sw,2}}{dt} = -i\Delta\omega a_{sw,2}(t) - i|\beta|a_{sw,2}(t). \tag{5.19}$$

From these equations, we see that the standing wave modes resonate at frequencies $\pm|\beta|$ detuned from the original resonance frequency.

For cavity QED applications, one very important consequence of the distinction between traveling wave and standing wave modes is in the effective volume of the mode V_{eff}. Standing wave WGMs have approximately half the volume of the traveling wave WGMs, so that the coupling rate g between a single quantum dot and a single photon in a standing wave cavity mode is expected to be $\sqrt{2}$ times that when the quantum dot is coupled to a traveling wave cavity mode. This of course assumes the single QD is positioned at an antinode of the standing wave mode; alternately, if it happens to be positioned at a node, the coupling rate g will be zero. Chapter 8 considers the coupling of a QD to standing wave modes in a microdisk in much greater detail, invoking quantum master equation simulations [149] to aid in the analysis.

5.3 Fabrication

The specific devices we consider are AlGaAs/GaAs microdisk cavities with embedded quantum dots (QDs). The epitaxy used was grown by Professors Andreas Stintz and Sanjay Krishna at the Center for High Technology Materials (CHTM) at the University of New Mexico, and is shown in table 5.1. It consists of a single layer of InAs quantum dots embedded in an InGaAs quantum well [144], which is in turn sandwiched between layers of AlGaAs and GaAs to create a 255 nm thick waveguide. This DWELL (short for dot-in-a-well) material has a room temperature ground state emission peak at around 1190 nm (fig. 5.1(b)), and is grown on top of a 1.5 μm $Al_{0.70}Ga_{0.30}As$ layer that eventually serves as a support pedestal for the microdisk.

The cavities are created through: (i) deposition of a 200 nm SiN_x mask layer, (ii) electron beam lithography and subsequent reflow of the e-beam resist to produce smooth and circular patterns, (iii) SF_6/C_4F_8 inductively coupled plasma reactive ion etching (ICP-RIE) of the deposited SiN_x mask layer (fig. 5.2(a)), (iv) Ar-Cl_2 ICP-RIE etching of the $Al_{0.3}Ga_{0.7}As$ layer and removal of the remaining SiN_x layer, (v) photolithography and isolation of the microdisk onto a mesa stripe that

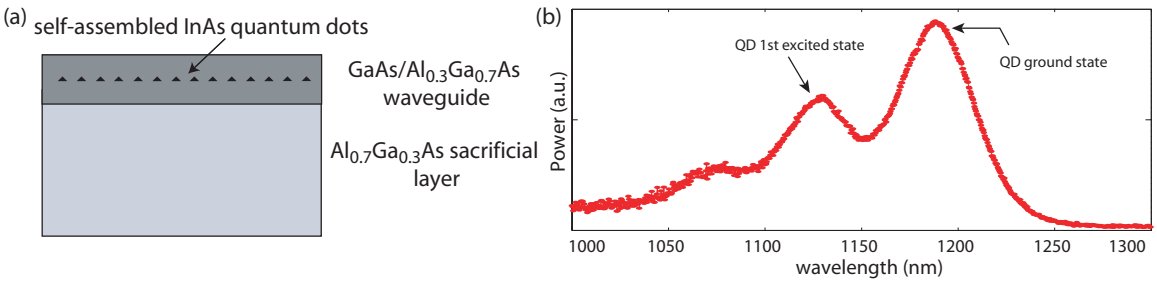

Figure 5.1: (a) Schematic of the DWELL epitaxy from which microdisk cavities are formed. (b) Photoluminescence from an unprocessed region of the 1DWELL material.

Table 5.1: Epitaxy for 1-DWELL microcavity lasers.

Layer	Materials	Thickness
Surface cap layer	GaAs	100 Å
Top waveguide layer	$Al_{0.30}Ga_{0.70}As$	400 Å
Top waveguide layer	GaAs	740 Å
Quantum well layer	$In_{0.15}Ga_{0.85}As$	60 Å
Quantum dot layer	InAs	2.4 monolayer
Barrier layer	$In_{0.15}Ga_{0.85}As$	10 Å
Bottom waveguide layer	GaAs	740 Å
Bottom waveguide layer	$Al_{0.30}Ga_{0.70}As$	500 Å
Sacrificial buffer layer	$Al_{0.70}Ga_{0.30}As$	15000 Å
Substrate	GaAs	N/A

is several microns above the rest of the chip (fig. 5.2(d)), and (vi) HF acid wet chemical etching of the underlying $Al_{0.7}Ga_{0.3}As$ layer to form the supporting pedestal (fig. 5.2(b)-(c)). The e-beam lithography and SiN_x etch steps are particularly important, as any roughness in the mask layer is transferred into the AlGaAs region. A resist reflow process originally developed for use with Si microdisks [65] is employed to create an initial mask pattern that is as circular as possible, and the subsequent SiN_x etch has been calibrated to produce as smooth a sidewall surface as possible (fig. 5.2(a)), without particular concern for its verticality. The subsequent Ar-Cl_2 etch is highly selective so that the angled mask does not result in erosion of the AlGaAs sidewalls. The fabricated

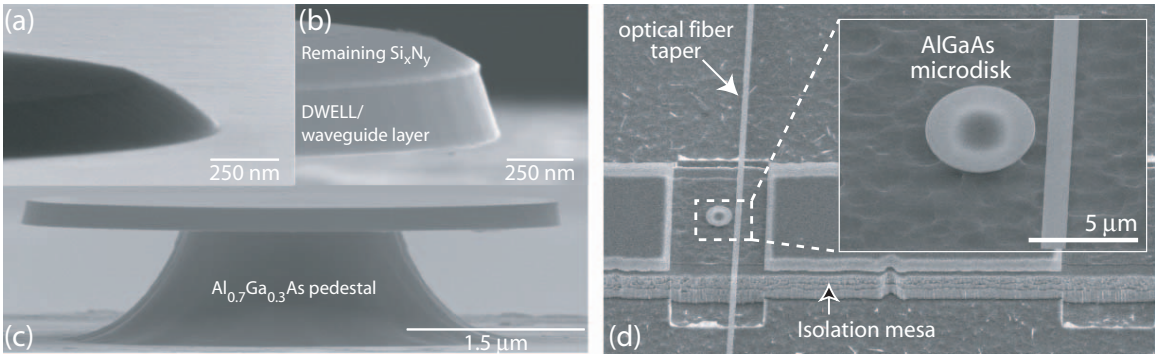

Figure 5.2: Scanning electron microscope (SEM) images of DWELL-containing microdisk cavities after the (a) SiN_x etch, and (b)-(c) AlGaAs etch and undercut. (d) Fully processed device, showing the isolation mesa that is incorporated in order to aid in the taper testing. An optical fiber taper aligned to the side of a microdisk is also visible in this image.

microdisks studied in this chapter are $D \sim$4.5 μm in diameter.[2] Additional fabrication details are given in appendix C.

5.4 Cavity Q measurements in the 1400 nm band

Initial passive measurements to measure the cold-cavity Q factor of the microdisk resonant modes were performed using the optical-fiber-based evanescent coupling technique. As was the case for measurements of the PC cavities in chapter 4, the optical fiber taper is formed by heating and adiabatically stretching a standard single mode fiber until it reaches a minimum diameter of ~ 1 μm. A fiber-coupled scanning tunable laser ($<$ 5 MHz linewidth) operating in the 1400 nm band is spliced to the taper's input, and when the taper is brought within a few hundred nanometer (nm) of the cavity, their evanescent fields interact, and power transfer can result. A schematic illustrating the coupling geometry for this system is shown in fig. 5.3(a). The devices are tested in the 1400 nm band because it is significantly red detuned from the QD spectrum (fig. 5.1), so that absorption due to the DWELL layer will be negligible at these wavelengths.

The Q of a cavity mode is determined by examining the linewidth of the resulting resonance in the taper's wavelength dependent transmission spectrum. In fig. 5.3(b), we show a doublet resonance of a microdisk (D=4.5 μm, 1-DWELL structure) in the 1400 nm wavelength band when

[2]The AlGaAs sidewalls do show a pronounced angle; this angle does reduce the maximum achievable (radiation-limited) Q of the cavity modes, but for TE-like modes, this reduction does not prevent the devices from exhibiting radiation-limited Qs in excess of 10^8 (for $D \sim 4.5$ μm), even in the presence of the slant. As surface roughness is expected to be a more serious source of loss, the tradeoff between smoothness and verticality is acceptable.

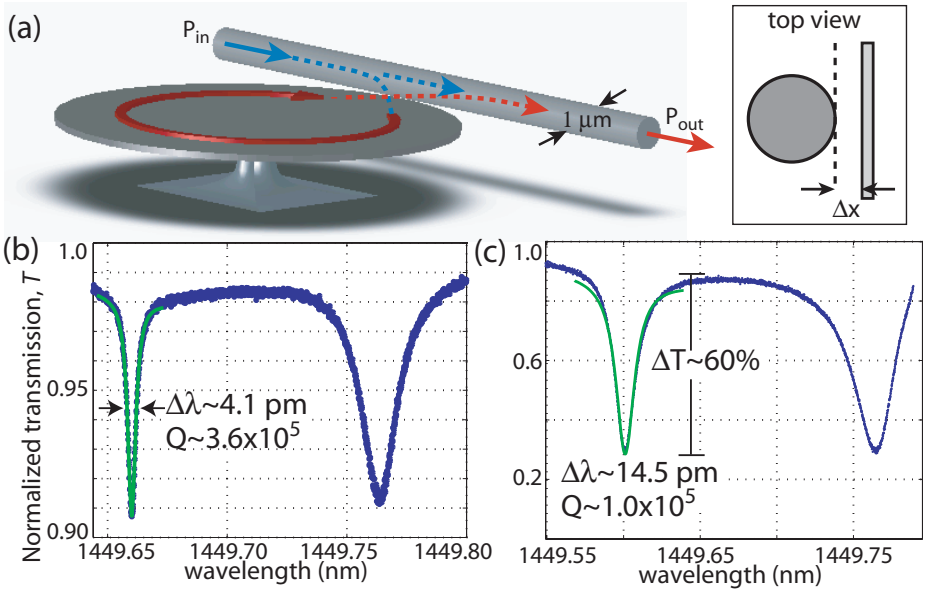

Figure 5.3: (a) Schematic geometry for probing the microdisk cavities through side-coupling via an optical fiber taper. (b) Normalized taper transmission ($T = P_{out}/P_{in}$) of a 4.5 μm diameter microdisk for a taper-disk lateral separation (Δx) of $\sim$ 800 nm. (c) Normalized taper transmission for the same device with $\Delta x \sim$ 200 nm. The overlying solid green curves are Lorentzian fits to the data.

the taper is $\sim$ 1 μm to the side of the disk; the separation is kept large in order to reduce taper loading effects [52, 64]. The double resonance peaks correspond to standing wave modes formed from mixtures of the degenerate clockwise and counterclockwise whispering gallery modes that couple and split due to the disk-edge surface roughness [64, 148, 146], as discussed earlier within the chapter. The linewidth ($\Delta\lambda$) of the shorter wavelength resonance corresponds to $Q \sim 3.6\times10^5$. Similarly, in fig. 5.3(c), we show the spectral response of the doublet when the taper is positioned much closer ($\sim$ 200 nm) to the edge of the disk, so that the amount of coupling has increased. The combination of increased coupling as well as parasitic loading due to the presence of the taper has increased the total loss rate of the resonant mode, yielding a loaded $Q \sim 1.0\times10^5$. The depth of coupling, however, has also considerably increased from 10% to 60%, corresponding to a photon collection efficiency η_0 (the ratio of "good" coupling to all other cavity losses including parasitic and intrinsic modal loss) of approximately 20% (see appendix E for the exact definition of η_0). It is believed that the high Q values achieved in these measurements are due to a combination of the resist reflow process that reduces radial variations and subsequent Rayleigh scattering in the disk, and the optimized dry etching processes that create very smooth disk-edge sidewalls.

The demonstrated Q is high enough that, if used in cQED, the cavity will have a decay rate

$\kappa/2\pi \sim 0.35$ GHz (at $\lambda \sim 1.2$ μm), lower than the aforementioned typical low temperature QD dipole decay rate of $\gamma_\perp/2\pi \sim 1$ GHz. After adjusting for the reduced wavelength of the QD resonance, the current devices (D=4.5 μm) have a $V_{\text{eff}} \sim 6(\lambda/n)^3$ for the standing wave resonant modes studied here.[3] For a maximally coupled InAs QD (spontaneous emission lifetime $\tau \sim 1$ ns, oscillator strength $f \sim 18$ [110]), this mode volume corresponds to $g/2\pi \sim 11$ GHz (refer to Appendices D and H for the formulas used to calculate κ and g). Thus, even for the disk sizes considered here, an appropriately positioned QD would place the system deep within the strong coupling regime. Of additional importance is the fiber-based coupling technique used here. This method allows for the Q to be accurately determined in a way that does not rely upon the (weak) background emission from the QDs [70, 71, 72]; all that is required is a probe laser that can be slightly detuned from the QD absorption lines. Furthermore, the taper also acts as a coupler that transfers light from an optical fiber into the wavelength-scale mode volume of the cavity, where it can interact with the QDs, and as a subsequent output coupler. Such integration could markedly improve the collection efficiency in cavity QED experiments, particularly important for microdisk and photonic crystal cavities, which typically do not have a radiation pattern that can be effectively collected by free-space optics or a cleaved fiber [71]. Subsequent chapters further discuss the advantages of using the fiber taper coupler in such experiments.

5.5 Initial measurements of lasing behavior

In addition to the fiber-based passive measurements of the microdisks at $\lambda \sim 1.4$ μm, we performed some initial room temperature photoluminescence measurements to study the QD emission in the 1.2 μm wavelength band. The cavities (D=5 μm in this case) were optically pumped at room temperature using a pulsed 830 nm semiconductor laser, and the emitted laser light was collected by a microscope objective and spectrally resolved in an optical spectrum analyzer (OSA). The setup that was used was essentially identical to that used in chapter 3. Initial measurements were performed on cavities containing 3 DWELLs due to their higher modal gain, roughly three times that of a single DWELL layer [144]. Emission is observed for a small number ($\sim$2-5) of modes in a given microdisk (fig. 5.4(a)). Figure 5.4(b) shows a typical light-in-light-out (L-L) curve for a 3-DWELL device pumped with a 300 ns period and 10 ns pulse width; the device exhibits lasing action with an estimated threshold value of $\sim$22 μW.

[3] Our estimate of κ assumes that $Q \sim 3.6\times10^5$ is achievable at $\lambda \sim 1200$ nm. In chapter 6, we present measurements that show that such Qs are indeed achievable at the shorter wavelengths.

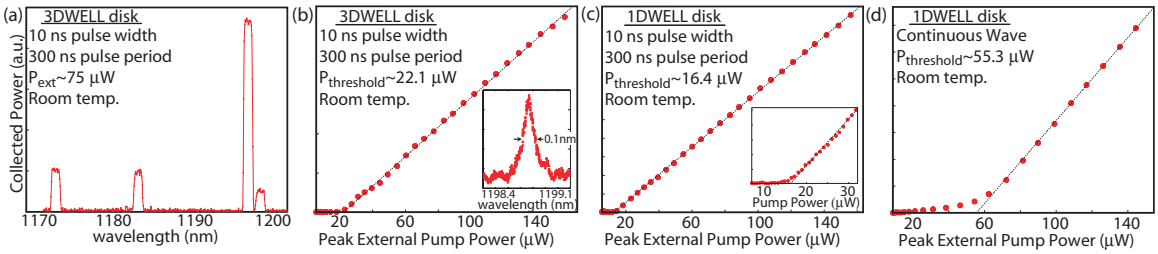

Figure 5.4: (a) Photoluminescence spectrum of a 3-DWELL microdisk device (OSA resolution bandwidth (RBW)= 1 nm). (b)-(d) L-L curves for: (b) pulsed 3-DWELL microdisk laser (inset shows the subthreshold spectrum of a cavity mode), (c) pulsed 1-DWELL microdisk laser (inset shows L-L curve near threshold), and (d) 1-DWELL microdisk laser under CW pumping conditions. The dashed lines are least-square linear fits to the above-threshold data.

The saturated ground state modal gain for single DWELL structures has been estimated to be $\sim$ 3.6-5.4 cm^{-1} [144, 150]. Noting that modal gain approximately equals modal loss at threshold, this indicates that a *minimum* cavity $Q \sim$ 3-5 $\times 10^4$ is required for this single layer of QDs to provide enough gain compensation to achieve lasing. The fiber-based linewidth measurements described earlier indicate that such Q factors should be achievable, and indeed, lasing from the QD ground states is observed in these single dot layer devices (fig. 5.4(c)). The laser threshold pump power for the 1-DWELL devices was measured to be as small as 16.4 μW, significantly lower than the 750 μW threshold values recently reported for similarly sized microdisk QD lasers [151]. Furthermore, as shown in fig. 5.4(d), continuous wave (CW), room temperature lasing was also obtained, albeit with a somewhat higher laser threshold.

The laser threshold values we report here are the peak pump powers incident on the sample surface; the absorbed power is estimated to be roughly 16% of this value, determined by calculating the expected reflectivities at the disk interfaces and assuming an absorption coefficient of 10^4 cm^{-1} in the GaAs and quantum well layers [152]. The threshold absorbed pump power for the 1-DWELL lasers is thus $\sim$ 2.6 μW. From this, the equivalent threshold current density, useful for comparing the performance of the microdisk lasers to previously demonstrated broad-area stripe lasers, can be estimated. Given the pump spot size ($\sim$ 16 μm^2), and assuming an internal quantum efficiency $\sim$ 1, we arrive at an equivalent threshold current density of 11 A/cm^2 for the 1-DWELL devices. In comparison, the estimated *transparency* current density in previous work on broad-area 1-DWELL lasers was 10.1 A/cm^2 [144]. The proximity of the demonstrated laser threshold to this transparency value indicates that non-intrinsic optical losses within the microdisk cavity have largely been eliminated.

In conclusion, AlGaAs microdisks as small as 4.5 μm in diameter and supporting standing wave

resonant modes with Q factors as high as 3.6×10^5 in the 1400 nm wavelength band have been demonstrated. These cavities contain integral InAs quantum dots, and initial room temperature photoluminescence measurements have yielded laser threshold values as low as 16.4 μW, nearing the transparency level of the material. In the following chapters, we will extend this work along two primary fronts: (i) use of the fiber taper within the photoluminescence measurements as a means to effectively collect (and source) light from the cavities, thereby creating fiber-coupled lasers, and (ii) consideration of smaller diameter disks, where the additional size reduction is important from the standpoint of increasing the peak electric field strength within the devices, to push cavity QED experiments further within the regime of strong coupling.